Passive remote sensing of the atmospheric boundary layer in Colorado's East River Valley during the seasonal change from snow-free to snow-covered ground

Bianca Adler[1,2], James Wilczak,[2], Laura Bianco[1,2], Ludovic Bariteau[1,2], Christopher J. Cox[2], Gijs de Boer[1,2,3], Irina Djalalova[1,2], Michael Gallagher[1,2], Janet M. Intrieri[2], Tilden Meyers,[4]Timothy Myers[1,2], Joseph B. Olson[5], Sergio Pezoa[1,2], Joseph Sedlar[1,6], Elizabeth Smith[7], David D. Turner[5], Allen White[2]

[1]Cooperative Institute for Research in Environmental Sciences (CIRES), University of Colorado Boulder
[2]NOAA Physical Sciences Laboratory, Boulder CO
[3]IRISS, University of Colorado, Boulder CO
[4]NOAA Air Resources Laboratory, Boulder CO
[5]NOAA Global Systems Laboratory, Boulder CO
[6]NOAA Global Monitoring Laboratory, Boulder CO
[6]NOAA National Severe Storms Laboratory, Norman OK

Key Points:

- Temperature profiles retrieved from remotely sensed infrared radiances allow to study the valley boundary layer over different snow covers.
- The nocturnal inversion in a high-altitude mountain valley is mixed out under snow-free conditions and persists during daytime over snow.
- NOAA's operational weather prediction model struggles to correctly forecast the boundary layer likely due to the too coarse grid spacing.

Corresponding author: Bianca Adler, `bianca.adler@noaa.gov`

Abstract

The structure and evolution of the atmospheric boundary layer (ABL) under clear-sky fair weather conditions over mountainous terrain is dominated by the diurnal cycle of the surface energy balance and thus strongly depends on surface snow cover. We use data from three passive ground-based infrared spectrometers deployed in the East River Valley in Colorado's Rocky Mountains to investigate the response of the thermal ABL structure to changes in surface energy balance during the seasonal transition from snow-free to snow-covered ground. Temperature profiles were retrieved from the infrared radiances using the optimal estimation physical retrieval TROPoe. A nocturnal surface inversion formed in the valley during clear-sky days, which was subsequently mixed out during daytime with the development of a convective boundary layer during snow-free periods. When the ground was snow covered, a very shallow convective boundary layer formed, above which the inversion persisted through the daytime hours. We compare these observations to NOAA's operational High-Resolution-Rapid-Refresh (HRRR) model and find large warm biases on clear-sky days resulting from the model's inability to form strong nocturnal inversions and to maintain the stable stratification in the valley during daytime when there was snow on the ground. A possible explanation for these model shortcomings is the influence of the model's relatively coarse horizontal grid spacing (3 km) and its impact on the model's ability to represent well-developed thermally driven flows, specifically nighttime drainage flows.

Plain Language Summary

We investigated how the vertical temperature structure in a high-altitude mountain valley in Colorado's Rocky Mountains evolves over snow-free and snow-covered ground. The vertical temperature structure in valleys determines how well air and thus pollutants in the valley can be mixed with the air above and is thus decisive for air quality and human health. During the night, air near the surface cools more than air above leading to an increase of temperature with height, a so-called temperature inversion forms which suppresses vertical mixing. During the day, solar radiation warms the ground and vertically mixes the air in the valley. When the ground is snow-covered, the mixing is limited to a shallow layer of a few hundred meter depth adjacent to the surface and the nocturnal inversion persists above through the daytime hours trapping air in the valley. We compared the observations to NOAA's operational forecast model and found that minimum nighttime temperatures and daytime mixing were overestimated by the model, especially over snow-covered ground. We attributed the model errors to the relatively coarse horizontal grid spacing of 3 km, which suggests that a reduction of grid spacing in the operational model could improve the forecast accuracy in mountainous terrain.

1 Introduction

The atmospheric boundary layer (ABL) is the lowest part of the atmosphere that is directly affected by the Earth's surface (Stull, 1988). Over mountainous terrain under clear sky fair weather conditions, the evolution of its structure is forced by convection and thermally driven circulations (Zardi & Whiteman, 2013; Serafin et al., 2018), which, in turn, are influenced by diurnal and terrain-induced variability in surface radiation and energy balance. Nighttime radiative cooling and drainage flows (i.e. downslope and downvalley winds) lead to formation of a surface temperature inversion in valleys and basins, that is, a layer in which temperature increases with height. Depending on the magnitude of energy input at the surface during the day, the nocturnal temperature inversions may erode after sunrise, either due to the upward growth of a well-mixed convective boundary layer (CBL) and/or the descent of the inversion top (Whiteman, 1982). While the convective heating in snow-free valleys is usually sufficient to erode the nocturnal inversion (e.g. Herrera-Mejía & Hoyos, 2019; Adler, Gohm, et al., 2021), multi-

day low-level inversions may persist in snow-covered valleys with very shallow CBLs forming above the ground (e.g. Chemel et al., 2016; Largeron & Staquet, 2016a, 2016b; Adler, Wilczak, et al., 2021). During periods with strong persistent inversions, pollutants can accumulate in valleys with significant implications for air quality and human health (e.g. Lareau et al., 2013; Largeron & Staquet, 2016b). Over areas of continuous snow cover, average net radiation and sensible heat flux are often negative during wintertime (e.g. Cullen & Conway, 2015; Stigter et al., 2021; Mott et al., 2018) meaning that solar energy is reflected and the surface is emitting energy, primarily at longer (infrared) wavelengths. Over patchy horizontally heterogeneous snow cover, very large differences in albedo and surface fluxes occur on small scales, internal boundary layers form, and local advection of sensible heat becomes relevant (Mott et al., 2018).

Errors and uncertainties in mesoscale numerical weather prediction (NWP) models are usually amplified over mountainous terrain compared to flat terrain (Zhong & Chow, 2013, and references therein). One common problem is that nocturnal inversions in valleys are often too weak compared to observations, which may result in misrepresentation of the breakup of inversions during the day. Model performance largely depends on the specific configuration, including details related to horizontal and vertical grid spacing, domain extent, grid nesting, and the initial and boundary conditions applied. Also, the physical parameterizations employed, such as turbulence and boundary layer parameterizations, land surface models (LSM), land use data sets, and radiation models, play a central role in dictating model performance. One item that is known to be particularly problematic is the model's horizontal grid spacing, as coarse resolution limits the capability of the model to represent the detailed orographic structure of mesoscale valleys and tributaries. Additionally, terrain smoothing used in some NWP systems results in the underestimation of elevation differences between ridges and valley floors. Evaluating the configuration of a specific model is also impacted by coarse resolution, as the detailed observations required for such evaluation are often from instrumentation deployed to a single location. This is particularly problematic in areas of complex terrain, where there can be substantial variability in ABL conditions over very short distances. For example, large differences between simulated and observed ABL thermal structure may result if observational data collected on a valley floor is compared to the nearest model grid point, located on the adjacent slope. In general, high resolutions are required to accurately portray flows over complex terrain, in part due to the need to have multiple grid points present to detect features of interest. For example, to resolve flow features such as thermally driven winds, the feature scale should be 6-8 times the horizontal grid spacing according to Skamarock (2004) and Skamarock and Klemp (2008). This means that models with a grid spacing on the order of 2-3 km would not be able to adequately capture features of less than 15 km in scale.

Much of the research on the ABL structure and evolution in snow-covered valleys is based on *in situ* measurements on surface towers or airborne platforms such as radiosondes and tethersondes. While the latter give detailed information on the vertical structure of the ABL, the measurements are not continuous and only provide snapshots. This can be problematic in areas where atmospheric conditions evolve at time scales significantly shorter than those observed by these platforms. Great potential to gain a deeper insight in the evolution of the vertical thermal ABL structure comes from ground-based remote sensing instruments such as passive microwave radiometers and infrared spectrometers and active water vapor absorption lidars (Turner & Löhnert, 2021), which provide continuous information on the profiles of temperature and humidity. Such instruments have been successfully deployed to study, for example, the summertime ABL in a valley on the mountainous island of Corsica (Adler & Kalthoff, 2014), the wintertime ABL in a snow-covered valley in the French Alps (Chemel et al., 2016), and the ABL in a tropical valley in the Colombian Andes (Herrera-Mejía & Hoyos, 2019). The evaluation of NWP models in mountainous terrain is often based on near-surface measurements only, as these measurements are widespread and readily available. However, im-

portant quantities like ABL depth and thermal stratification can only be evaluated against profile measurements which emphasizes the value of continuous remotely sensed profiles for NWP model evaluation. By utilizing both types of observations, Adler, Wilczak, et al. (2022) evaluated the representation of a wintertime persistent cold air pool in different versions of the National Oceanic and Atmospheric Administration (NOAA) operational High-Resolution-Rapid-Refresh (HRRR) model.

In this study, we investigate the response of the ABL thermal vertical structure to changes in the energy balance at the surface during the seasonal transition from snow-free to snow-covered ground in a high-altitude valley using continuous remotely sensed temperature profiles. We then compare these observations to the operational HRRR model to evaluate the model performance and investigate possible reasons for model errors. To clearly isolate the response of the ABL to changes in snow cover and to avoid complicating factors such as low-level clouds or synoptically-driven flows, we focus on completely clear-sky days. Our research questions are grouped into two sets of questions, with the first focused on process understanding, and the second focused on model evaluation: (i) What is the vertical thermal structure of the ABL under different snow-cover conditions and how does that structure change along the valley? How do the nocturnal temperature inversion, CBL, and stratification in the valley atmosphere vary temporally and spatially? (ii) How well does the operational HRRR model capture the conditions in the valley? Do the model errors depend on the time of the day, snow cover, and meteorological situation, and do they vary along the valley?

To address these questions, we use data from a collaborative research initiative currently ongoing in the East River Watershed of Colorado. This work includes efforts associated with the National Oceanic and Atmospheric Administration (NOAA) Study of Precipitation, the Lower Atmosphere, and Surface for Hydrometeorology (SPLASH, NOAA Physical Science Laboratory, 2021b) and the U.S. Department of Energy (DOE) Atmospheric Radiation Measurement (ARM) program Surface Atmosphere Integrated Field Laboratory (SAIL, Feldman et al., 2021) campaigns. The main focus of the SPLASH initiative is to enhance weather and water prediction capabilities by measuring, evaluating, and understanding integrated atmospheric and hydrologic processes relevant to water resources. The East River Watershed is a representative mountainous headwater catchment of the Colorado River Basin, which is a primary source of water for much of the southwestern United States. As part of the multi-year SPLASH and SAIL field campaigns, three passive remote sensing infrared spectrometers were deployed simultaneously along the axis of the East River Valley for a three-month period from the end of October 2021 to the end of January 2022, covering the seasonal change from snow-free to snow-covered ground. To our knowledge, this is the first time such an instrument combination is used to study the spatio-temporal characteristics of the ABL in a high-altitude valley. To obtain temperature profiles from infrared spectrometers, we use an optimal estimation physical retrieval (i.e. Tropospheric Remotely Observed Profiling via Optimal Estimation (TROPoe Turner & Löhnert, 2014; Turner & Blumberg, 2019; Turner & Löhnert, 2021). We then compare the observations to model output at the grid point closest to the stations to investigate model errors under different snow-cover conditions.

The manuscript is structured as follows: Section 2 describes the investigation area as well as the observational and model data. In Sect. 3, the temporal evolution of observed near-surface conditions, including radiation and energy balance components during the whole 3-month period, is analyzed (Sect. 3.1). This is followed by an investigation of the observed diurnal cycle of the ABL on a day-to-day basis at one site (Sect. 3.2) and along the valley axis using 24-h composites (Sect. 3.3). In Sect. 4, the ABL thermal structure in the HRRR model is evaluated (Sect. 4.1) and possible reasons for the model errors are discussed (Sect. 4.2).

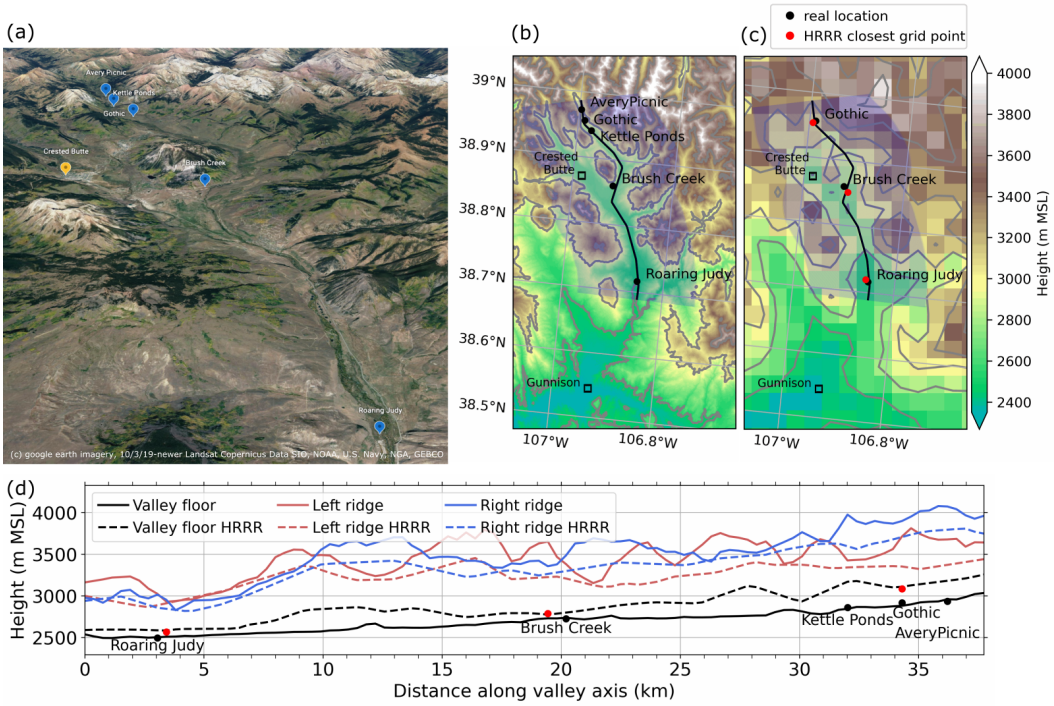

Figure 1. (a) Google earth imagery of the investigation area. Terrain height (b) based on 30-m resolution elevation data from the Shuttle Radar Topography Mission and (c) as used in the operational HRRR model with 3 km grid spacing. (d) Elevation of the valley floor and ridges (left and right of the valley axis when looking upvalley) computed from SRTM and HRRR elevation data along the axis of the East River Valley indicated by the black line in (b) and (c). The shaded polygon in (b) and (c) marks the area used for the estimates of the ridge heights. Black and red dots in (b)-(d) indicate the location and heights of the sites in the real world and in the HRRR model grid.

2 Investigation area, observational, and model data

The study area is the East River Valley, which is embedded in the East River Watershed and located near Crested Butte and Gunnison in Colorado's Rocky Mountains (Fig. 1a,b). The land cover type is a mix of evergreen and deciduous forest, grasslands, and barren land (Xu et al., 2022). The distance along the valley axis from the measurement site furthest down the valley (Roaring Judy) to the site furthest up the valley (Avery Picnic) is around 35 km (Fig. 1). All measurement sites are on the valley floor. The valley floor rises from around 2500 m above mean sea level (MSL) at Roaring Judy to nearly 3000 m MSL at Avery Picnic. The valley depth on average is more than 500 m and the flat part of the valley floor ranges in width from a few kilometers at its widest part to less than 1 km near the Kettle Ponds, Gothic, and Avery Picnic sites.

While the valley orography is much smoother in the 3-km HRRR model configurations, the primary features of the valley are still resolved (Fig. 1c). To characterize the ridge height on both sites of the valley floor in the observations and simulations, we manually defined a valley axis (black line in Fig. 1b,c) and extracted elevation data along slices perpendicular to the valley axes spanning 10 km on each side. For each slice and each side of the valley we determined the maximum elevation value. Figure 1d shows the elevation of the valley floor and ridges in reality (solid lines) and in the HRRR model (dashed lines). As can be expected due to the coarse model resolution, valley depth is reduced in the model compared to reality. In an automated near-real time routine, model data at the grid points closest to the real-world locations of the sites (red dots in Fig. 1c) are extracted from the operational HRRR forecasts. We evaluated the HRRR data at Gothic, Brush Creek and Roaring Judy, since these are the sites where continuous temperature profiles from the TROPoe retrievals were available. The extracted model grid points for these sites are on the simulated valley floor (Fig. 1c,d).

2.1 Observational data

2.1.1 Thermodynamic profilers

Three ground-based infrared spectrometers were deployed along the axis of the East River Valley at Gothic, Brush Creek, and Roaring Judy during the three-month investigation period from 21 October 2021 to 28 January 2022. At Gothic, an Atmospheric Emitted Radiance Interferometer (AERI Knuteson et al., 2004b, 2004a) is operated as part of the second ARM Mobile Facility (AMF2) deployed for the SAIL campaign (Feldman et al., 2021). A second AERI was deployed at Brush Creek as part of the Collaborative Lower Atmospheric Mobile Profiling System (CLAMPS) system (Wagner et al., 2019). A third infrared spectrometer at Roaring Judy was an Atmospheric Sounder Spectrometer by Infrared Spectral Technology (ASSIST Rochette et al., 2009) operated by NOAA's Physical Science Laboratory. The AERI and ASSIST generally have the same functionality, construction, and operating principles. While the AERI at Gothic and the ASSIST at Roaring Judy were operated during the whole study period, the AERI at Brush Creek was taken down 10 days earlier on 18 January to support a separate field campaign.

The AERI and ASSIST are passive spectrometers that receive downwelling infrared radiation between the wavelengths of 3.3 and 19 μm (520-3000 cm^{-1}) at a spectral resolution of about 0.5 wavenumber (Knuteson et al., 2004b, 2004a). The instruments have a hatch that closes during precipitation events to protect the fore optics, which inhibits measurements during rain or snow. We retrieved thermodynamic profiles every 10 min from the observed instantaneous radiances using the optimal estimation physical retrieval TROPoe (Turner & Löhnert, 2014; Turner & Blumberg, 2019; Turner & Löhnert, 2021). The spectral bands used in the retrieval are in the wavenumber range from 612 - 905.4 cm^{-1} and are specified in Turner and Löhnert (2021). Additional input data in TROPoe are cloud base height from a colocated ceilometer, temperature and water vapor mixing ratio from near-surface measurements and from hourly analysis profiles from the op-

erational Rapid Refresh (RAP, Benjamin et al., 2016) weather prediction model at the closest grid point. The latter are used only outside the ABL above 4 km above ground level (AGL) and provide information in the middle and upper troposphere where little to no information content is available from the infrared radiances. In addition to these temporally resolved input data, TROPoe requires an a priori dataset (*prior)* which provides mean climatological estimates of thermodynamic profiles and specifies how temperature and humidity covary with height as an input (for details see e.g. Djalalova et al., 2022). The prior is a key component of the retrieval and provides a constraint on the ill-posed inversion problem. For this study, we computed the prior from operational radiosondes launched near Denver, CO, and re-centered the mean profiles of water vapor and temperature to account for the elevation difference between the East River Valley and the launch site near Denver to get a more representative prior (for details see Appendix Appendix A).

The retrieval determines the optimal state vector, which consists of thermodynamic profiles, and satisfies both the observations, RAP profiles above 4 km AGL, and the prior. The state vector includes temperature and water vapor profiles with 55 vertical levels each from the surface up to 17 km, with the distance between levels starting at 10 m and increasing with height, as well as liquid water path. Starting with the mean prior as a first guess of the state vector, a forward model is used to compute pseudo-observations, which are then compared to the actual observations. The retrieval iterates until the differences between the pseudo-observations and the observations are small within a specified uncertainty. As the forward model, we use the Line-By-Line Radiative Transfer Model LBLRTM (Clough & Iacono, 1995; Clough et al., 2005).

Before running TROPoe, a principal component noise filter is applied to the infrared radiances to reduce the random error (Turner et al., 2006). Ideally, uncertainties in the observations, prior, and forward model are propagated and characterized by the posterior covariance matrix. Because including the uncertainty of the forward model would increase the computational costs of the retrieval substantially, we assume the uncertainty of the forward model is zero and inflate the uncertainty associated with the observed radiances by using the radiance uncertainty before noise filtering is applied (for details see Turner & Blumberg, 2019). Because the AERI performs longer sky averages than the ASSIST, the radiance uncertainty of the AERI is lower and we found that it was not sufficient to compensate for the missing uncertainty in the forward model, resulting in an overfitting of the profiles. We hence further increased the noise in the AERI radiances by multiplying the radiance uncertainties with a factor for which the retrieved temperature profiles best agreed with the radiosonde profiles (for details see Appendix Appendix B).

2.1.2 Surface observations

Measurements of 2-m temperature and horizontal wind speed and direction were obtained at five sites along the valley axis, including Avery Picnic, Gothic, Kettle Ponds, Brush Creek, and Roaring Judy. Wind measurement heights were 3.8 m AGL at Avery Picnic, 10 m AGL at Gothic, 3 m AGL at Kettle Ponds and Brush Creek, and 4 m AGL at Roaring Judy. Measurement heights refer to snow-free ground, the growing snowpack reduced the height separation between sensor and surface through the season. Up- and downwelling longwave and shortwave radiation flux components as well as 30-min sensible heat fluxes were measured at the upper four sites, Avery Picnic, Gothic, Kettle Ponds, and Brush Creek, and precipitation measurements were used from Gothic. In this study, net radiation is positive when directed downwards towards the surface and sensible heat flux is positive when directed upwards away from the surface.

All data at Gothic were collected with AMF2. At the other sites, we utilized data from Atmospheric Surface Flux Stations (ASFS, Cox et al. (2023)) at Avery Picnic and

Kettle Ponds (sensible heat flux only) and from mobile SURFRAD-like stations (Butterworth et al., 2021; Sedlar et al., 2022) at Brush Creek and Kettle Ponds for radiation, cloud properties, and meteorology. To estimate albedo we averaged shortwave downward and shortwave upward radiation fluxes when the solar zenith angle was less than 85 ° before computing the ratio. At Gothic and Brush Creek, measurements of direct and diffuse solar radiation were available to compute shortwave downward radiation fluxes (McArthur, 2005), while at the other sites we used broadband fluxes. Details on the platforms and sensors can be found in the meta data for the individual data sets (see Data Availability section).

2.1.3 Radiosondes

As part of the AMF2 deployment, radiosondes were launched twice daily at 5 and 17 MST (0 and 12 UTC) at Gothic, providing thermodynamic and wind profiles throughout the troposphere. The radiosonde profiles were used to re-center the prior (Appendix Appendix A), to help determine the optimal uncertainty configuration for the AERIs (Appendix Appendix B), and to compute different ABL quantities (Sect. 3.3). When comparing the radiosonde profiles to TROPoe retrieved profiles, we first interpolated the radiosonde profiles to the same height levels as the retrieved profiles to avoid differences arising from the higher vertical resolution of the sonde.

2.1.4 Ceilometer

Four ceilometers manufactured by Vaisala were deployed at Gothic, Kettle Ponds, Brush Creek, and Roaring Judy measuring attenuated aerosol backscatter profiles with a temporal resolution of less than 1 min. In this study, we used the first cloud-base height, as determined using Vaisala's CL-view software, to identify clear-sky and cloudy days. At each site, we computed a daily cloud-base fraction for cloud bases below 3 km AGL. We required it to be less than 5 % at all sites for a day to be considered clear-sky and we identified cloudy days for which the temporal low-level cloud-base fraction was larger than 50 % at any of the sites.

2.1.5 Terra satellite

To get information on the temporal evolution of spatial snow coverage in the area, we used the normalized difference snow index (NDSI) from MODIS on-board of the Terra satellite (Hall & Riggs, 2021). Snow-covered surfaces typically have a very high reflectance in visible bands and very low reflectance in shortwave infrared bands. The NDSI reveals the magnitude of this difference. NDSI is available daily on a regular grid with 500 m spacing. We computed a mean daily NDSI for the investigation area when valid NDSI data are available for at least 50 % of the pixels and not obscured by clouds.

2.2 HRRR model data

We evaluated the currently operational version of NOAA's HRRR weather prediction model (version 4, Dowell et al., 2022) with a horizontal grid spacing of 3 km by comparing the observations to the closest grid point in the model (Fig. 1c). The operational HRRR model is initialized hourly with a forecast horizon of 19 h. Every 6 hours, the forecast horizon is extended to 48 h. For this study, we used hourly model output from the 48-hr forecasts which were initialized at 0, 6, 12, and 18 UTC. For each of these initialization times, we split the 48-hr forecasts in half and concatenated the first and last 24 hours of the forecasts, illustrated in Fig. 2. This resulted in the development of a continuous time series of model data for the different configurations (i.e., eight in total with four initialization times and forecast periods 0-23 and 24-47), which we could compare against the observations. With this method, discontinuities in model data resulted at

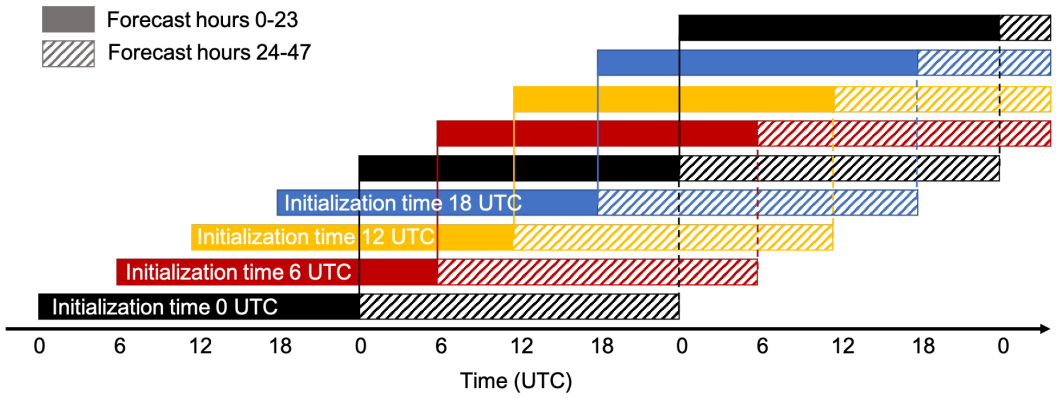

Figure 2. Illustration of the eight different configurations which are used to develop continuous time series of the HRRR model data. The different colored boxes indicate blocks of 24 h of data from runs initialized at different times, which are then concatenated to get continuous time series. Solid boxes indicate data from forecasts hour 0 to 23 and hatched boxes from 24-27.

the initialization times when the model data shifted from one forecast run to the next. We evaluated the model for all eight configurations and found that the main conclusions are similar for each configuration. Because of this, we decided to mostly show results from the first 24 hours of the forecasts initialized at 6 UTC (red boxes in Fig. 2).

Hourly model data were compared against instantaneous observation nearest in time with a maximum tolerance of 10 min, and simulated profiles were linearly interpolated to the measurement heights. Because wind observations were not performed at 10 m AGL at Brush Creek and Roaring Judy, the simulated 10-m horizontal wind data were reduced to the actual wind measurement height at the respective site assuming a logarithmic wind profile.

We computed 24-h composites of bias and mean absolute error (MAE) of temperature T as:

$$Bias = \frac{1}{n}\sum_{i=1}^{n}(T_{i,\mathrm{model}} - T_{i,\mathrm{obs}}) \tag{1}$$

$$MAE = \frac{1}{n}\sum_{i=1}^{n}|T_{i,\mathrm{model}} - T_{i,\mathrm{obs}}| \tag{2}$$

with n being the number of samples available at each hour of the day, T_{obs} being the observed temperature, and T_{model} being the simulated temperature.

3 Observed evolution of the ABL during the seasonal snow cover change

3.1 Near-surface conditions

Significant changes in near-surface conditions occurred during the three-month observation period (Fig. 3) and these can clearly be linked to the snow cover. Smaller snowfall events during the first half of the period (Fig. 3c) led to temporary increases in albedo (Fig. 3f), but this snow melted quickly and therefore did not result in an area-wide snow cover, as the mean NDSI values remained less than 20 % (Fig. 3d). This changed with a multi-day snowfall event between 6 and 10 December, after which the albedo increased to values larger than 0.9 and the mean NDSI remained above 60 % through the end of the investigation period in January. Using albedo and NDSI as criteria for snow cover,

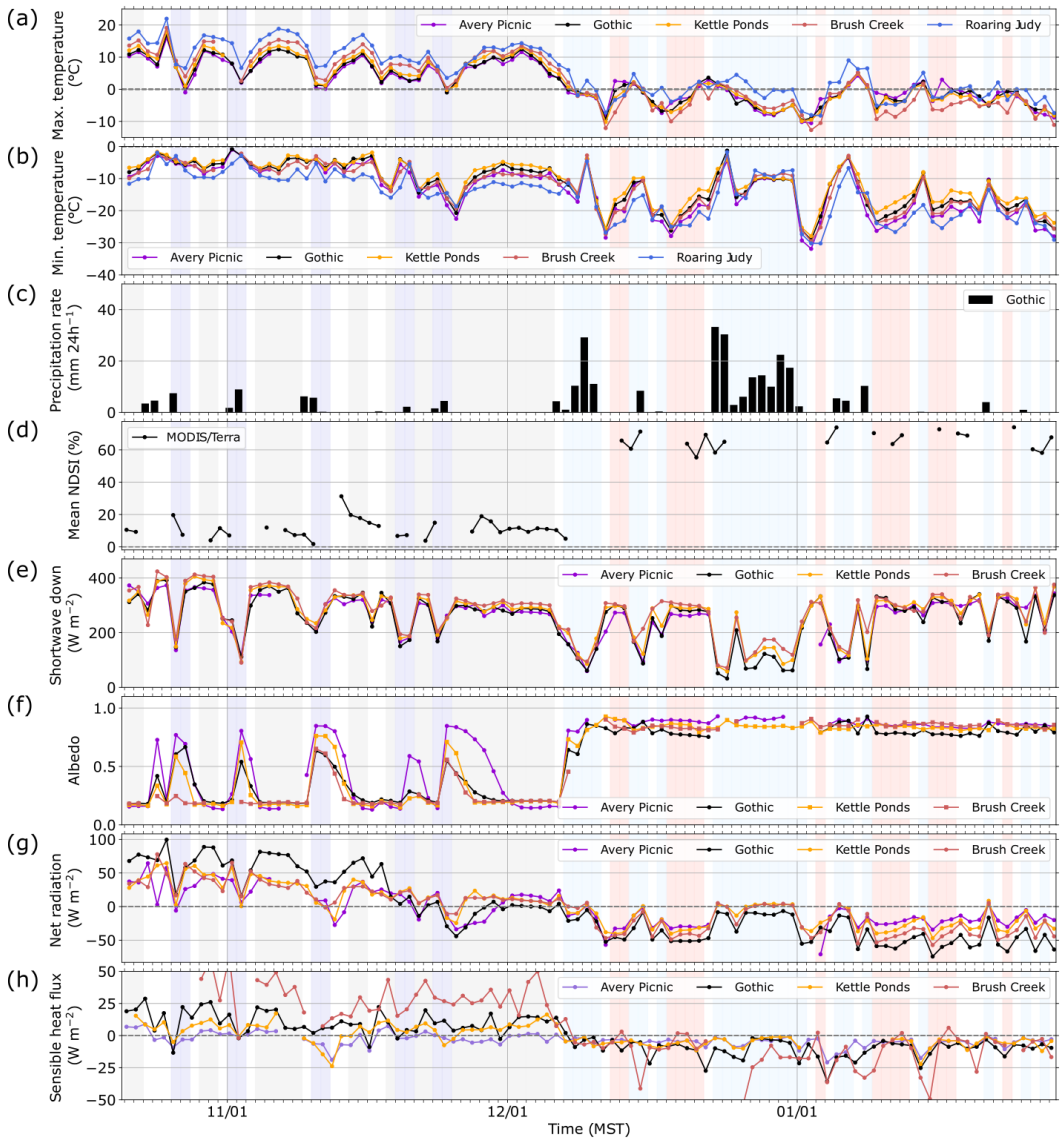

Figure 3. Daily (a) maximum and (b) minimum 2-m temperature, (c) daily precipitation rate, (d) domain mean normalized difference snow index (NDSI), (e) daily daytime mean shortwave downward radiation flux, (f) albedo at noon, (g) daily mean net radiation (positive when directed towards the surface), and (h) daily mean sensible heat flux (positive when directed away from the surface) during the 3-month investigation period. Grey and red shadings indicate clear-sky days and purple and blue shadings mark cloudy days during the snow-free and snow-covered regimes, respectively, determined using daily cloud-base fractions from ceilometers.

we split the observational period into two regimes. This includes a *snow-free* regime including and up to 6 December, during which any snow cover was patchy, intermittent, and heterogeneous, and a *snow-covered* regime including and following 7 December, during which a large fraction of the surface was continuously covered by snow. Visible camera images taken automatically at Gothic, Kettle Ponds, and Brush Creek confirmed the snow-cover change (not shown).

For both regimes, we identified clear-sky and cloudy days using cloud-base heights from the four ceilometers deployed along the valley axis (Sect. 2.1.4). Clear-sky days during the snow-free and snow-covered regime are indicated by gray and red shading and cloudy days by purple and blue shading in Fig. 3. During a few of the identified clear-sky days, mid-or high-level clouds occurred but were found to have a small impact on solar radiation (Fig. 3e).

Daily mean solar radiation on clear-sky days decreased before and increased after the winter solstice (Fig. 3e). This may explain the gradual decrease of daily mean net radiation (Fig. 3g) and daily maximum temperature (Fig. 3a) during the snow-free regime. Under snow-covered conditions, daily mean net radiation remained negative, even as one gets further away from winter solstice. Daily mean surface sensible heat flux dropped to negative values under snow-covered conditions (Fig. 3h), that is, it was directed towards the surface compensating for some of the surface radiative cooling (Fig. 3g). While maximum daytime temperatures regularly reached more than 10 °C under snow-free conditions at all sites, they generally did not exceed 0 °C on clear-sky days under snow-covered conditions (Fig. 3a). Minimum nighttime temperatures during clear-sky days were mostly between -5 to -10 °C under snow-free conditions, but regularly dropped below -20 °C under snow-covered conditions (Fig. 3b).

While the primary changes in near-surface conditions during the transition from snow-free to snow-covered ground generally occurred at all sites alike, differences are visible between the sites on individual days which demonstrate the impact local terrain features can have on the surface energy balance components and air temperature. For example, the higher mean sensible heat fluxes at Brush Creek under snow-free conditions (Fig. 3h) were likely related to local site characteristics such as more rocks, more exposed aggregate, and fewer grass than at the other sites as well as its vicinity to a steep slope. Independent of snow cover, the overall lowest nighttime temperatures on clear-sky days were measured at Roaring Judy (Fig. 3b), that is the site furthest down the valley and lowest in altitude (Fig. 1) which is an indication of an extensive cold air pool filling the whole valley and which will be investigated in more detail in (Sect. 3.3). Despite being only a few kilometers apart from each other (Fig. 1d), minimum nighttime temperatures at the three sites furthest up the valley differed by several degrees with Avery Picnic measuring the lowest temperature (Fig. 3b). While the sites at Gothic and Kettle Ponds were not at the lowest point of the valley floor, the site at Avery Picnic was in close proximity to the river and a small-scale terrain depression likely favored the formation of a local cold pool at this site.

3.2 Diurnal cycle of the ABL

After having investigated daily mean, minimum and maximum values in Sect. 3.1, we now focus on the diurnal cycle of the ABL through the snow-cover transition using measurements at Roaring Judy as an example (Fig. 4), as this was the site with the greatest and most continuous data availability for temperature profiles (Fig. 5a,b). While the 2-m temperature on clear-sky days was overall lower under snow-covered conditions compared to snow-free conditions, a clear diurnal cycle was visible during both (Fig. 4a). Temperature started to increase about one hour after sunrise and started to decrease about one hour before sunset. Note that sunrise and sunset times were computed using the ge-

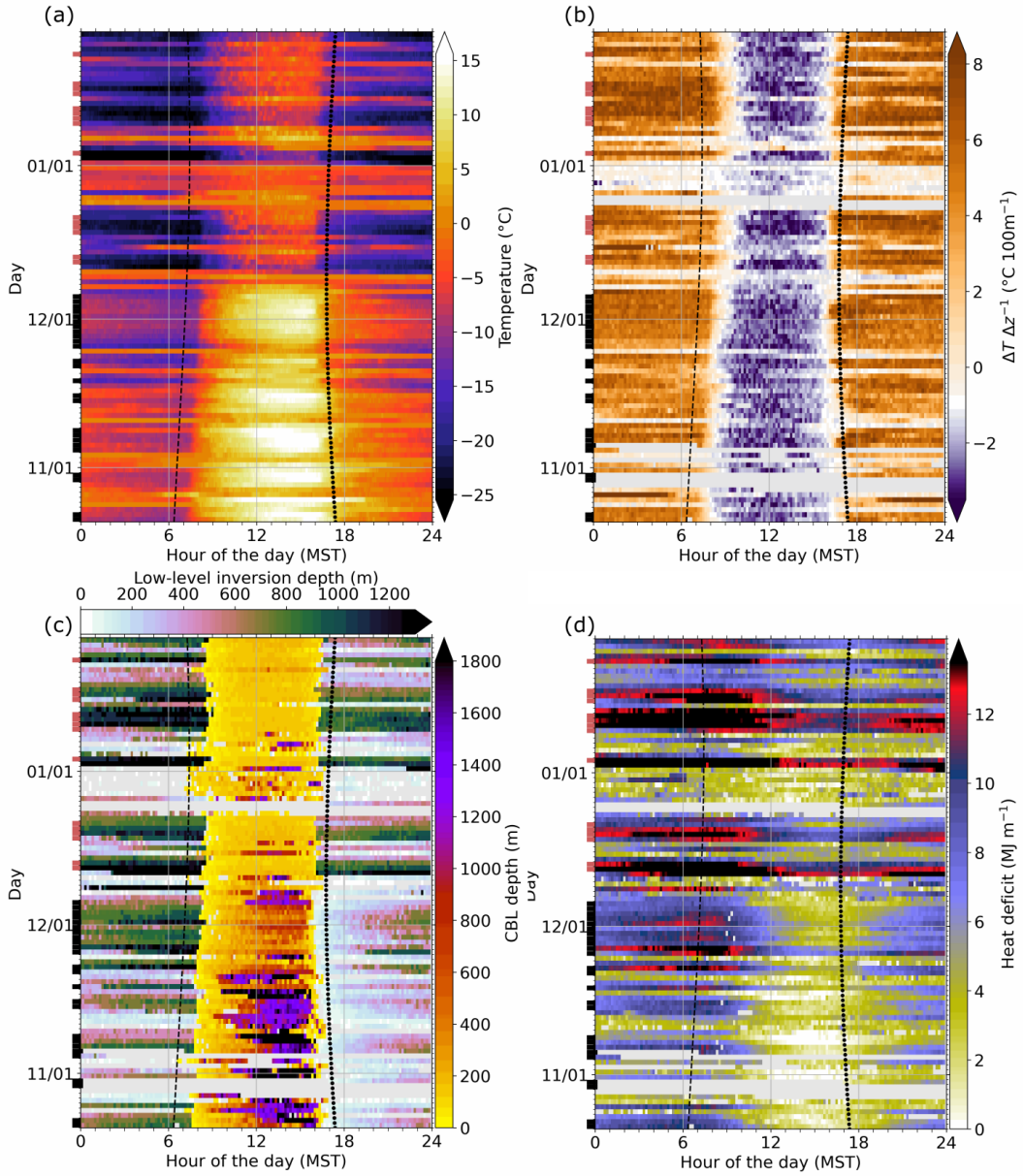

Figure 4. Daily evolution of (a) 2-m temperature, (b) temperature gradient over the lowest 100 m above ground, (c) CBL depth determined between sunrise and sunset using the parcel method and depth of the low-level inversion defined as the layer adjacent to the surface in which temperature increases with height, and (d) heat deficit computed after Eq. 3 at Roaring Judy. Besides the 2-m temperature, all quantities are computed using thermodynamic profiles retrieved with TROPoe. The dashed and dotted lines indicate sunrise and sunset, respectively. Black and red bars at the left y-axis indicate clear-sky days under snow-free and snow-covered conditions, respectively.

ographic location and do not consider local topographic impacts like shading from valley sidewalls.

Associated with the decrease in 2-m temperature shortly before sunset, a surface inversion regularly formed during clear-sky days as indicated by positive temperature gradients in the lowest 100 m AGL (Fig. 4b). Temperature gradients were typically around 5 to 6 °C 100 m^{-1} and did not change much throughout the night. During the day, an unstable layer evolved near the surface, which was similar in strength (around -2 to -3 °C 100 m^{-1}) under both snow-cover conditions. The CBL, however, was much deeper under snow-free conditions (Fig. 4c). Its depth was computed between sunrise and sunset using the parcel method (Seibert et al., 2000), that is we determined the height at which the surface value of virtual potential temperature matched the virtual potential temperature profile. Duncan Jr. et al. (2022) found a good agreement for CBL depth estimates with the parcel method when using radiosonde and AERI-based TROPoe retrieved profiles.

The temporal evolution and depth of the stably stratified layer varied considerably with snow cover (Fig. 4c). We defined a low-level inversion as the layer adjacent to the surface in which temperature increased with height and determined its depth as the height above ground where temperature started to decrease. Under snow-free conditions, an inversion gradually formed, reaching average maximum depths of around 900 m in the early morning. In contrast when the ground was snow covered, an inversion of around 750 m depth on the average was detected as soon as the unstable layer near the surface diminished, preventing the detection of a CBL. This indicates that the very shallow CBL under snow-covered conditions was topped by a deep stably-stratified layer which connected to the surface-based inversion as soon as convection stopped. This will be investigated more in Sect. 3.3.

As a proxy for the stratification in the valley, we computed the heat deficit Q (Whiteman et al., 1999) from the surface (h_{sfc}) up to 4000 m MSL (this is the height above which we no longer found diurnal temperature changes, Sect. 3.3):

$$Q = c_p \int_{h_{\mathrm{sfc}}}^{4000} \rho(z)\,[\theta_{4000} - \theta(z)]\,dz \tag{3}$$

where c_p is the specific heat capacity of air at constant pressure, $\rho(z)$ is the air density profile, θ_{4000} is the potential temperature at 4000 m MSL, and $\theta(z)$ denotes the potential temperature profile. With a station height of 2494 m MSL, the layer depth over which Q is computed amounts to 1500 m for Roaring Judy. Q describes the heat required to mix out the stable stratification below 4000 m MSL and to obtain a well-mixed layer with height-constant potential temperature. Small values indicate that the stratification is close to well-mixed, while large values are a sign of very stable layering. The temporal evolution of the heat deficit describes if stable layers are built, maintained or destroyed. Under snow-free conditions, the heat deficit showed a clear diurnal cycle with low values during daytime and high values during the night (Fig. 4d), reflecting the evolution of the CBL (Fig. 4c) which eroded the inversion during daytime and the build-up of the low-level inversion during nighttime. The heat deficit still generally decreased during the day under snow-covered conditions, which can be attributed to the formation of the shallow CBL (Fig. 4c) and upper-level warming (see Sect. 3.3), but the values remained much higher indicating that the stable layer was far from being mixed out. The persistent stable layer in the valley was washed out several times by synoptically-driven systems indicated by low heat deficit values (Fig. 4d), for example during the period between 24 December and 1 January, a period with heavy snowfall (Fig. 3b), but quickly rebuilt under clear-sky conditions.

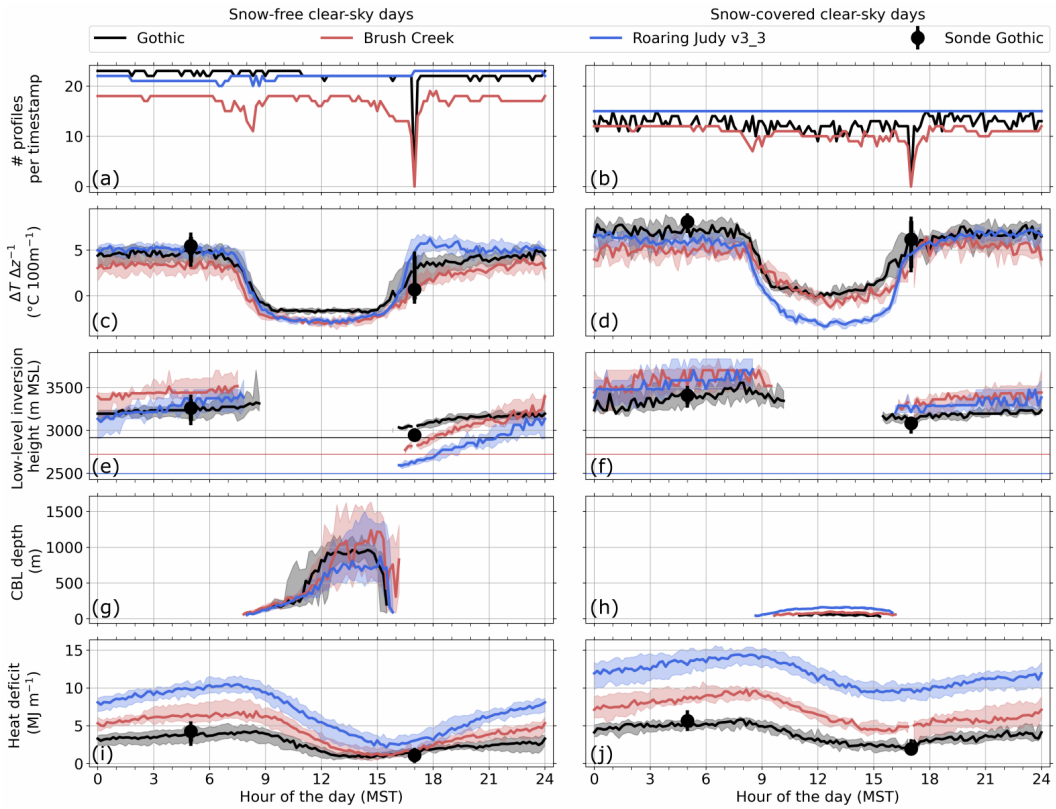

Figure 5. (a,b) Number of temperature profiles available for the analysis at each time stamp. 24-h median composites of (c,d) temperature gradient over the lowest 100 m AGL, (e,f) height of the low-level inversion defined as the layer adjacent to the surface in which temperature increases with height, (g,h) CBL depth determined between sunrise and sunset using the parcel method, and (i,j) heat deficit computed after Eq. 3 at Gothic, Brush Creek, and Roaring Judy for clear-sky days under snow-free (left column) and snow-covered (right column) conditions. In (c-j), shading marks the interquartile range. In (e,f), the thin horizontal lines indicate the respective station height. The black markers show quantities retrieved from the radio soundings at Gothic, all other quantities are computed using thermodynamic profiles retrieved with TROPoe.

Some of the changes we see in ABL conditions between both snow-cover regimes (Fig. 4) may be related to the reduction in solar radiation as one gets closer to winter solstice (Fig. 3d). However, the very abrupt changes right after the snowfall event ended on 10 December and the fact that the CBL depth remained low and the inversion remained deep even after solar radiation increased again in January, provide convincing evidence that the changes were dominated by snow cover strongly reflecting solar radiation and not by solar insolation.

3.3 Average ABL evolution along the valley axis

To compare the ABL evolution at the three sites Roaring Judy, Brush Creek, and Gothic along the valley axis (Fig. 1), we computed 24-h composites for clear-sky days under snow-free and snow-covered conditions of temperature profiles (Fig. 6) and, to provide a quantitative analysis, of low-level stability, low-level inversion height, CBL depth, and heat deficit (Fig. 5).

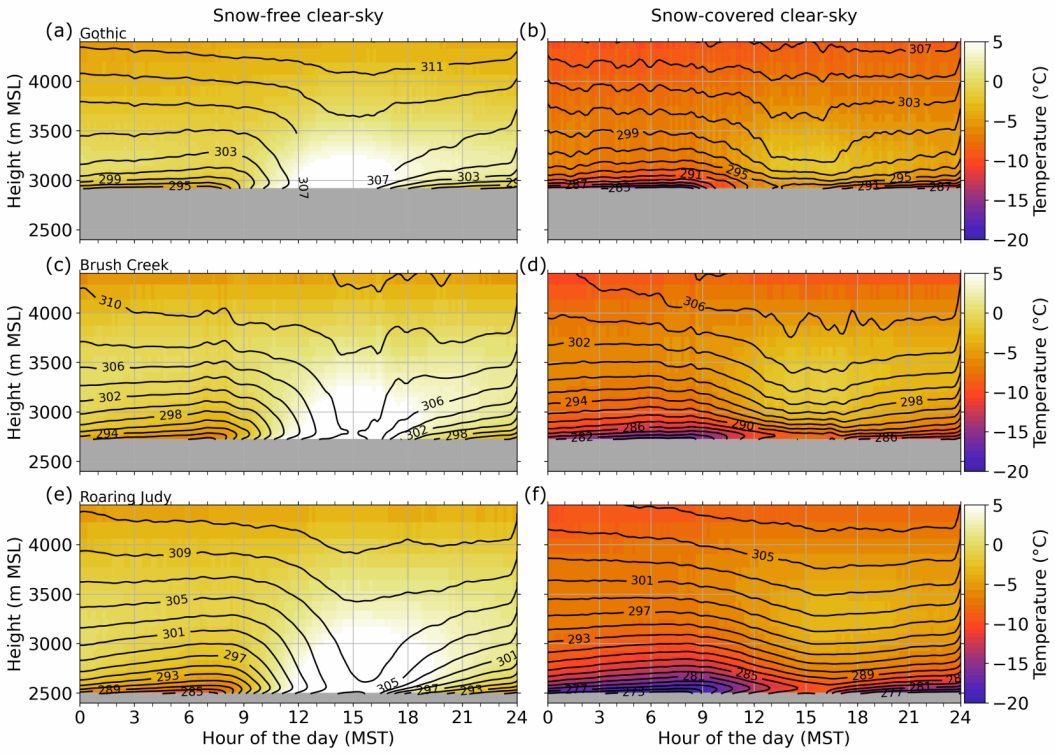

Figure 6. 24-h mean composites of temperature (color-coded) and potential temperature (isolines) profiles for clear-sky days under snow-free conditions (a,c,e) and snow-covered conditions (b,d,f) at Gothic (top row), Brush Creek (middle row), and Roaring Judy (bottom row). The thermodynamic profiles are retrieved with TROPoe.

The composite temperature profiles nicely show the much colder temperatures under snow-covered conditions (Fig. 6). The stratification in the valley was strongly stable at all sites during the night, independent of snow cover. A surface inversion started forming in the late afternoon indicated by an increase in the low-level temperature gradient (Fig. 5c,d). After the initial increase, the temperature gradients were nearly constant throughout the night and similar at all sites with values larger by approximately 1-2 °C 100 m^{-1} during the snow-covered regime. Under snow-free conditions, the inversion deepened gradually with time at all sites (Figs. 5e, 6a,c,e) with the strongest increase occurring during the first half of the night. After the initial growth, the inversion was quite stationary and very similar at all sites with respect to mean sea level indicating that a layered cold pool formed in the East River Valley with the coldest air accumulating at the lowest parts of the valley. Under snow-covered conditions, no gradual increase in inversion depth was detected at any of the sites at the beginning of the night, but immediately occurred at around 3200 m MSL on the average (Fig. 5f). During its stationary phase, the inversion height was between around 3200 and 3700 m MSL which roughly coincided with ridge heights in the area (Fig. 1b,d). The temporal evolution of the low-level inversion is well reflected in the heat deficit with values increasing gradually during the night (Fig. 5i,j). Heat deficit values are largest at Roaring Judy, because this is the lowest altitude site and the inversion depth is largest and strongest here temperature increasing by 10 °C under snow-free conditions and 15 °C under snow-covered conditions from the surface to the top of the inversion (Fig. 6e,f).

Distinct differences in ABL structure are visible during daytime depending on snow cover. Under snow-free conditions, a well-mixed CBL developed equally at all sites after sunrise reaching maximum depths of around 800 to 1000 m (Fig. 5g). It eroded the nocturnal temperature inversion in the valley (Fig. 6a,c,e) and resulted in near-zero heat deficit values in the afternoon (Fig. 5i). On the contrary, a very shallow CBL of less than 150 m depth developed under snow-covered conditions Fig. 5h). Above the CBL, the valley atmosphere remained strongly stably stratified (Fig. 6b,d,f) causing the high heat deficit values during the day (Fig. 5j). This also explains why no gradual increase in inversion depth was detected at the beginning of the night (Fig. 5f). The thermal structure of the ABL in the East River Valley under snow-covered conditions is very similar to the one found during wintertime in Alpine Valleys near Grenoble in the French Alps (Largeron & Staquet, 2016b, 2016a).

Even though the CBL was very shallow (Fig. 5h) and most of the valley atmosphere remained stably stratified during daytime (Fig. 6b,d,f), the heat deficit still decreased under snow-covered conditions (Fig. 5j). This can be related to a warming of the stably stratified valley atmosphere up to around 4000 m MSL (Fig. 6b,d,f) associated with a descent of the inversion top. This warming can be attributed to subsidence heating when the core of the valley subsides compensating for upslope flows carrying mass up the sidewalls (Whiteman, 1982). The inversion breakup mechanisms we found in the East River Valley, namely the upward growth of a CBL under snow-free conditions and the subsidence heating under snow-covered conditions, are consistent with the mechanisms proposed by Whiteman (1982). While we did not find observational evidence for a descending top of the inversion under snow-free conditions, it may exist, but might not be detectable due to the coarse vertical resolution of the retrieved profiles and the retrieval's inability to detect sharp elevated inversions (Djalalova et al., 2022). Unfortunately, no radio soundings were available during daytime to further investigate this.

4 Representation of the ABL in the HRRR model

4.1 Temperature errors

To evaluate the representation of the thermal ABL structure in the HRRR model, we computed 24-h mean composites of bias (Eq. 1) and MAE (Eq. 2) of 2-m temper-

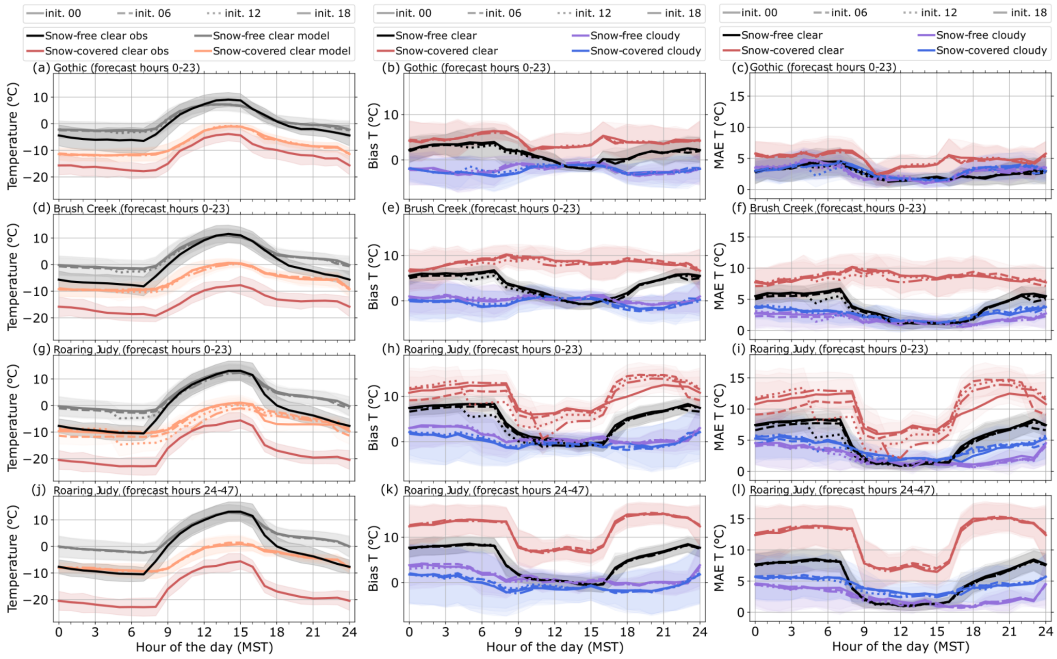

Figure 7. 24-h mean composites of (a,d,g,j) observed and simulated 2-m temperature and (b,e,h,k) bias and (c,f,i,l) mean absolute error (MAE) between simulated and observed 2-m temperature (model - observations) at Gothic, Brush Creek and Roaring Judy for clear-sky days under snow-free and snow-covered conditions. (a-i) show data from forecast hours 0-23 and (j-l) from forecast hours 24-47. The line style indicates different initialisation times (init.). Bias and MAE are additionally shown for cloudy days. The shading indicates the standard deviation.

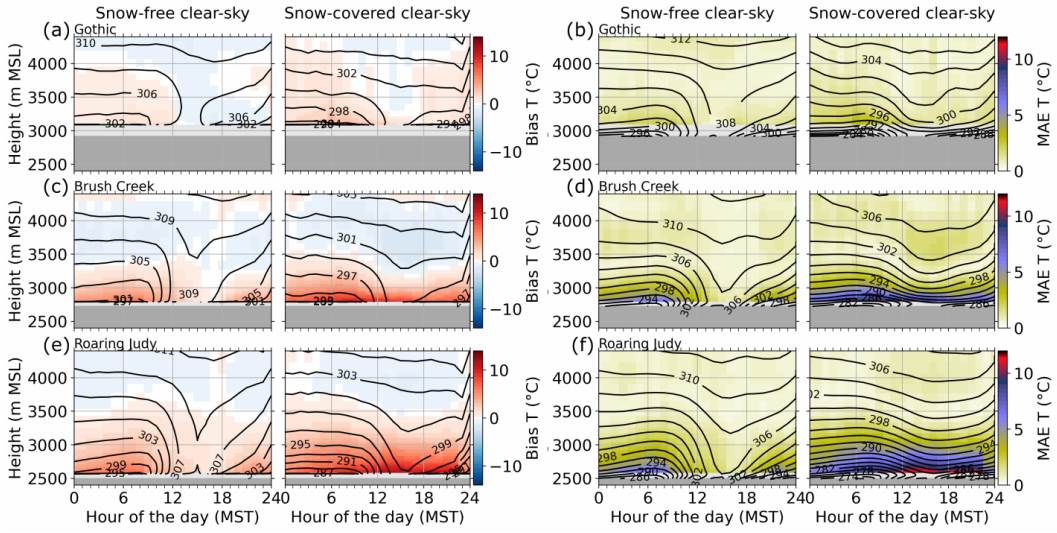

Figure 8. 24-h mean composites of (a,c,e) bias and (b,d,f) mean absolute error (MAE) profiles between simulated and observed temperature (model - observations) at Gothic, Brush Creek, and Roaring Judy for clear-sky days under snow-free and snow-covered conditions. The black isolines are 24-h mean composites of potential temperature simulated with the HRRR model (a,c,e) and retrieved with TROPoe (b,d,f). Model data for forecast hours 0-23 initialized at 6 UTC are shown. The dark grey shading indicates real world station height.

ature at Roaring Judy, Brush Creek, and Gothic (Fig. 7). On clear-sky days, the errors showed a diurnal cycle with lower values during the day and larger values during the night, except for Gothic. The errors were generally largest under snow-covered conditions. Model performance was worst at Roaring Judy with an average bias of up to 13 °C (Fig. 7h) and a MAE of up to 15 °C (Fig. 7i) during the night. The temporal evolution and magnitude of the errors at Gothic and Brush Creek were very similar for all initialization times (Fig. 7b,c,e,f). At Roaring Judy, however, the errors at a certain time of the day clearly depended on initialization time (Fig. 7h,i). The errors were generally lowest at the time of initialization and increased with forecast hour, as e.g. visible in the drops at 5, 11, and 23 MST under snow-covered conditions. For longer forecast hours (24-47 hours) the errors did not depend any more on initialization time, but were equally high and showed the same diurnal cycle (shown for Roaring Judy in Fig. 7j,k,l). Maximum errors for longer forecast hours were also not markedly higher than for the configurations using the first 24 forecast hours. This indicates that the time of initialization does not matter equally for all sites and that the model does not introduce ever growing errors with forecast length. Observed and simulated 2-m temperature indicates that nighttime cooling in the model, especially at the beginning of the night, is largely underestimated (Fig. 7a,d,g). After sunrise, the observed 2-m temperature increased more than the simulated one leading to a reduction in model errors, best visible at Roaring Judy. For comparison, we also computed the errors for cloudy days (indicated by blue and purple shading in Fig. 3). Biases for these days were near 0 °C or slightly negative and MAE was usually less than 5 °C, that is, much smaller than during clear-sky days.

The findings derived from the 2-m temperature errors generally hold for the temperature profiles as well. Figure 8 shows 24-hr mean composite profiles of bias and MAE as well as observed and simulated potential temperature isolines. The errors are computed with respect to mean sea level. Because terrain height at the individual sites was higher in the model than in the observations (Fig. 1d), the distance to the ground at a certain height was larger in the observations than in the model. In the presence of temperature inversions, computing the error profiles with respect to ground level would only lead to even larger MAE and positive biases than the ones shown in Fig. 8. Errors during clear-sky days were largest at lower altitude stations and increased towards the ground. This was clearly related to the failure of the model to correctly forecast the thermal stratification. Comparing observed (isolines in Fig. 8b,d,f) and simulated (isolines in Fig. 8a,c,e) potential temperature profiles revealed that the nocturnal strong surface inversions present in the observations at all sites independent of snow-cover were largely missing in the model. This has been identified as a common problem in NWP models (Zhong & Chow, 2013). Because the observed inversion was deepest and strongest at the lowest altitude site Roaring Judy (Fig. 8f), the impact of the erroneous stratification in the model was most pronounced here explaining the largest errors at this site (Figs. 7h,i and 8e,f). Under snow-free conditions, the warm bias and large MAE present during the night were much reduced or even absent during daytime with the formation of a well-mixed CBL in both the model and the observations. While in the observations a strongly stably stratified layer persisted above the shallow CBL during the day under snow-covered conditions (isolines in Fig. 8b,d,f), the valley atmosphere was only weakly stably stratified in the model (isolines in Fig. 8a,c,e) resulting in large model errors also during daytime.

4.2 Possible reasons for model errors during clear-sky days

The smaller model errors during cloudy days suggest that the errors during clear-sky days are related to one or more physical processes which are only present or most pronounced during clear-sky days and which are not correctly represented in the model. This could be thermally driven flows such as slope and valley winds which form and are most pronounced during clear-sky days. Another possible reason could be errors in the surface radiation budget.

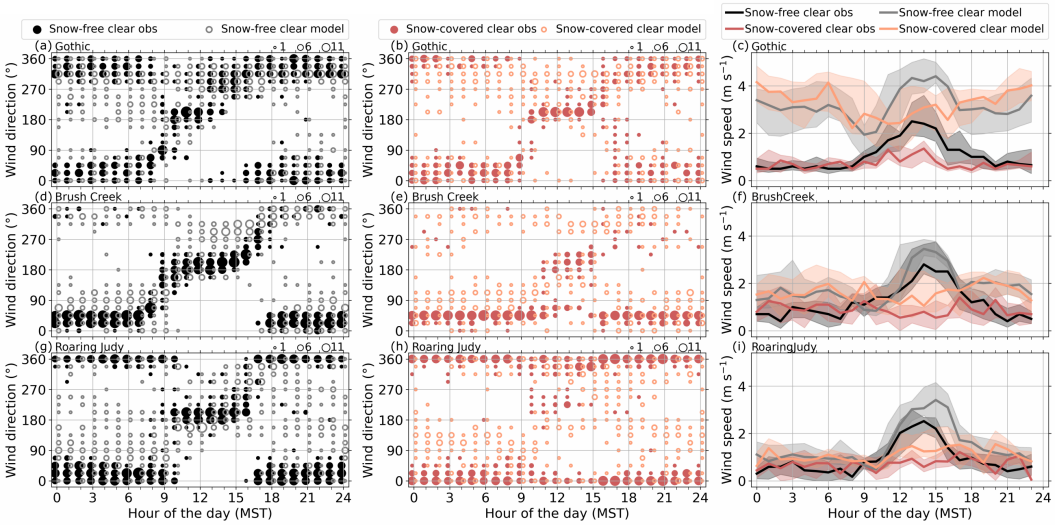

Figure 9. 24-h composites of observed and simulated near-surface (a,b,d,e,g,h) wind direction and (c,f,i) mean (solid line) wind speed at Gothic, Brush Creek and Roaring Judy for clear-sky and cloudy days under snow-free and snow-covered conditions. Model data from forecast hours 0-23 are shown. For wind direction, the marker size indicates how often a specific wind direction occurs at each time stamp using bins of 22.5 degree width. Model data for forecast hours 0-23 initialized at 6 UTC are shown. The shading in (c,f,i) indicates the standard deviation.

4.2.1 Thermally driven flows

We start with investigating the thermally driven flows by computing 24-h composites of near-surface wind speed and direction for clear-sky days (Fig. 9). Preferred wind directions are clearly visible in the observations at all three sites independent of snow cover. At Gothic, northwesterly to northeasterly flow prevailed during the night. Northwesterly flow indicates drainage along the main valley axis, while north-easterly flow was likely related to drainage outflow from a small tributary located to the north-east of Gothic (Fig. 1b). At Brush Creek and Roaring Judy, distinct downvalley wind along the main valley axis (oriented in north-easterly and northerly direction, respectively) dominated during the night. Southerly upvalley wind developed during daytime at all sites. It was more pronounced and lasted longer under snow-free conditions. When the ground was snow-covered, a shift to upvalley wind during daytime was not always observed on every day, especially at Roaring Judy and Brush Creek where downvalley wind sometimes persisted throughout the day. This lack of an upvalley wind during daytime is a common feature over glaciers or in snow-covered valleys (e.g. Obleitner, 1994; Whiteman, 2000; Song et al., 2007; Zardi & Whiteman, 2013).

Valley winds are driven by a horizontal pressure gradient along the valley axis which develops as a function of height between air columns with different vertical temperature structures in different sections of the valley (Zardi & Whiteman, 2013). During the day, the pressure at a given height is generally lower further up the valley causing an upvalley wind and vice versa during the night. The relationship between pressure difference and valley wind under clear-sky days was for example confirmed in the Inn Valley in Austria (Lehner et al., 2019) and the Adige Valley in Italy (Giovannini et al., 2017). We computed the horizontal pressure difference between Roaring Judy and Gothic after reducing the pressure at Roaring Judy to the altitude of Gothic for clear-sky days. Under snow-free conditions, we found a diurnal cycle of the pressure difference with Gothic having

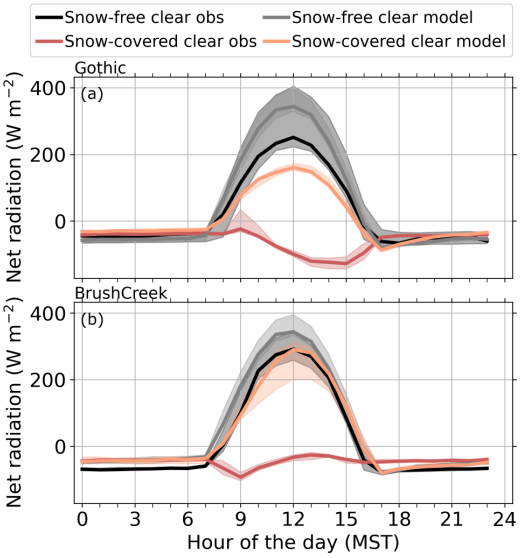

Figure 10. 24-h mean composites of observed and simulated net radiation at Gothic and Brush Creek for clear-sky days under snow-free and snow-covered conditions. Model data for forecast hours 0-23 initialized at 6 UTC are shown. The shading indicates the standard deviation.

lower pressure during the day and higher pressure during the night (not shown) which is consistent with the diurnal cycle in wind direction (Fig. 9a,d,g). Under snow-covered conditions, hardly any diurnal cycle in pressure difference was distinguishable which again agrees with the less distinct diurnal cycle in wind direction (Fig. 9b,e,f).

With the coarse model resolution, the fine-scale structure of the valley, such as the small tributary north-east of Gothic, is not resolved (Fig. 1c) and we did not expect the model to get all the details of the observed thermally driven flows right. Nevertheless, we were surprised by the absence of valley winds in the model data (Fig. 9). Wind direction was much more scattered than in the observations at all sites independent of snow-cover and a clear diurnal cycle was missing. The overestimation of near-surface horizontal wind speed especially visible at Gothic, may be an indication that stronger upper-level wind was able to penetrate into the weakly stably stratified valley atmosphere. The failure of the model to correctly simulate the nighttime drainage flows provides a possible explanation for the large errors in the ABL thermal structure (Sect. 4.1). Drainage flows transport cold high-density air that forms near the surface due to radiative cooling from higher parts of the valley to lower parts which leads to the accumulation of cold air on the valley floor and the buildup of a temperature inversion. The wind and temperature observations provide strong evidence that this was the main process responsible for the formation of the observed strong nocturnal inversions. We hypothesize that because drainage flows were largely missing in the model (Fig. 9), no strong nocturnal inversions could form and they were easily mixed out during daytime (Fig. 8). In particular under snow-covered conditions, this could lead to the very large errors in the layer where the stable stratification was maintained in the observations.

4.2.2 Surface radiation budget

An underprediction of radiative cooling at night could add to the warm nighttime biases. We therefore computed 24-h median composites of observed and simulated net

radiation under both snow-cover conditions at Gothic and Brush Creek (Fig. 10). No radiation measurements were available at Roaring Judy. Nighttime net radiation was negative and on the same order of magnitude in both the model and the observations, ruling out errors in the surface radiation budget as a relevant reason for the warm surface air temperature biases and too weak nighttime inversions in the model.

In contrast to nighttime, huge differences in net radiation are visible during daytime under snow-covered conditions. We found that this is largely related to an underprediction of albedo in the model over snow-covered ground, which was less than 0.55 in the model compared to more than 0.9 in the observations (Fig. 3e). While snow was present in the whole valley during the snow-covered regime as evident from satellite observations, snow frequently melted during daytime in the 24-h forecasts in the lower parts of the valley where simulated snow depth was lower. This indicates weaknesses in simulated snow-melting rates. The HRRR did not show a dry bias with respect to 2-m water vapor mixing ratio in the lower part of the valley (not shown). The warm bias, however, led to an underestimation of 2-m relative humidity which could enhance snow melt. The HRRR model uses the Rapid Update Cycle (RUC) LSM in which snow albedo depends on vegetation type, snow age, snow depth, snow cover, and snow temperature (Smirnova et al., 2016). Reasons for the erroneous representation of albedo and snow cover might be related to the missing representation of subgrid variability of snow in the current RUC LSM (He et al., 2021), biases introduced by the current data assimilation system (Benjamin et al., 2022; Dowell et al., 2022), or other potential errors in the physics parameterizations. He et al. (2021) showed that estimates of snow cover fraction are improved and surface heat fluxes are more realistic when coupling a stochastic snow model to the RUC LSM to represent the subgrid variability of snow. Modifications to both the land and atmospheric data assimilation system and to the RUC LSM will be addressed by the new Rapid Refresh Forecast System (RRFS), which is currently under development as part of NOAA's Unified Forecast System. It is expected that the RRFS will become the operational 3-km grid model, replacing the HRRR, in 2024.

Even though albedo differences are large and likely have implications for the land-atmosphere exchange during daytime and may contribute to the mix out of the simulated nighttime inversion, we do not think that they are the main reason for the large temperature errors. Instead we suspect the missing drainage flows. In a future study, we plan to run a nested simulation with smaller horizontal grid spacing to test if higher horizontal resolution allows to better simulate the thermally driven circulations in the East River Valley.

5 Summary and conclusions

In this study, we analyzed the response of the ABL to changes in the surface energy balance on clear-sky days during the seasonal transition from snow-free to snow-covered ground in the East River Valley near Crested Butte in Colorado's Rocky Mountains over a three-month period from October 2021 to January 2022. The simultaneous deployment of three infrared spectrometers provided a unique opportunity to study the thermal structure of the valley ABL. Temperature profiles were obtained from infrared spectrometer radiances using the optimal estimation physical retrieval TROPoe. We further evaluated NOAA's operational HRRR model with the observations to assess how well the model captures primary ABL characteristics under different snow-cover conditions.

The three-month observation period can roughly be divided in half, with mostly snow-free conditions during the first 6 weeks and snow-covered conditions after a multi-day snowfall event at the beginning of December. The changes in snow cover were associated with changes in observed surface albedo which increased from less than 0.3 to more than 0.9. Under snow-covered conditions, daily mean net radiation was directed

upwards from the surface indicating radiative cooling, sensible heat flux was directed downwards in turn compensating for some of the radiative cooling, and daily minimum and maximum 2-m air temperature values dropped with maximum values usually below freezing. Strong diurnal cycles in low-level air temperature were observed on clear-sky days throughout the whole period with the formation of a daytime CBL and a nocturnal surface inversion, which was strongest and deepest at the Roaring Judy site, located furthest down the valley. After an initial growth phase, the top of the inversion with respect to sea level was roughly the same at all three sites, indicating that a layered cold air pool filled the whole valley during nighttime. While the stable stratification in the valley was mostly mixed out during the day under snow-free conditions, a persistent inversion was present above a very shallow CBL under snow-covered conditions.

The HRRR model showed a large nocturnal warm bias in the ABL on clear-sky days (up to 13 °C at 2 m AGL under snow-covered conditions), because the model failed to form strong nocturnal inversions. The errors decreased with formation of the CBL during daytime. Unlike in the observations, where an inversion persisted above a very shallow CBL during the day under snow-covered conditions, much weaker simulated nighttime inversions were mostly mixed out, leading to large warm biases above the observed CBL in the valley atmosphere during daytime. The model errors were much smaller on cloudy days. We assert the main reason for the large temperature errors is a failure of the model to correctly simulate the thermally driven flows in the East River Valley. While nighttime drainage flows are a very clear and persistent feature in the observations, they are largely missing in the simulations. A future study will use a higher-resolution simulation to investigate if that inability of the HRRR to simulate the thermally driven flow was due to its 3-km grid spacing.

We showed that with careful processing, temperature profiles retrieved with TROPoe from ground-based passive remote sensing infrared spectrometers are suited to study the ABL evolution in complex terrain. With a temporal resolution of minutes, these retrievals are able to resolve diurnal changes in stratification under different snow-cover conditions. While we focused on clear-sky days only, temperature profiles can also be retrieved under cloud base and the response of lower tropospheric stability and subsequent surface energy fluxes to radiatively clear and cloudy conditions is the subject of another study (Sedlar et al. (n.d.)). The ABL plays a crucial role in the temporal evolution of seasonal snow cover, particularly during spring snowmelt. The continuous temperature profiles retrieved with TROPoe can provide invaluable information on the ABL thermal structure during the seasonal changes.

Retrieved temperature profiles proved further to be very useful for the model evaluation of ABL structure and stratification. From near-surface measurements alone we would not have been able to identify the problems the model has with simulating inversion strength and with maintaining the persistent inversion during daytime. The challenges faced by the model to correctly form and maintain inversions under snow-covered conditions can, for example, have implications for air quality forecasts in mountainous terrain.

Open Research Section

Measurements at Gothic are part of the Atmospheric Radiation Measurement (ARM) Mobile Facility (AMF2). The used data at Gothic are AERI radiances (Gero et al., 2021), radiosonde profiles (Burk, 2021), ceilometer cloud base height (Morris et al., 2021), radiation flux components (Shi, 2021b, 2021a), sensible heat flux (Sullivan et al., 2021), near-surface meteorological standard measurements (Keeler et al., 2021), and precipitation measurements (Cromwell & Bartholomew, 2021). NOAA Global Monitoring Laboratory conducted the ceilometer (NOAA Global Monitoring Laboratory, 2021b) and radiation (NOAA Global Monitoring Laboratory, 2021c) measurements at Kettle Ponds

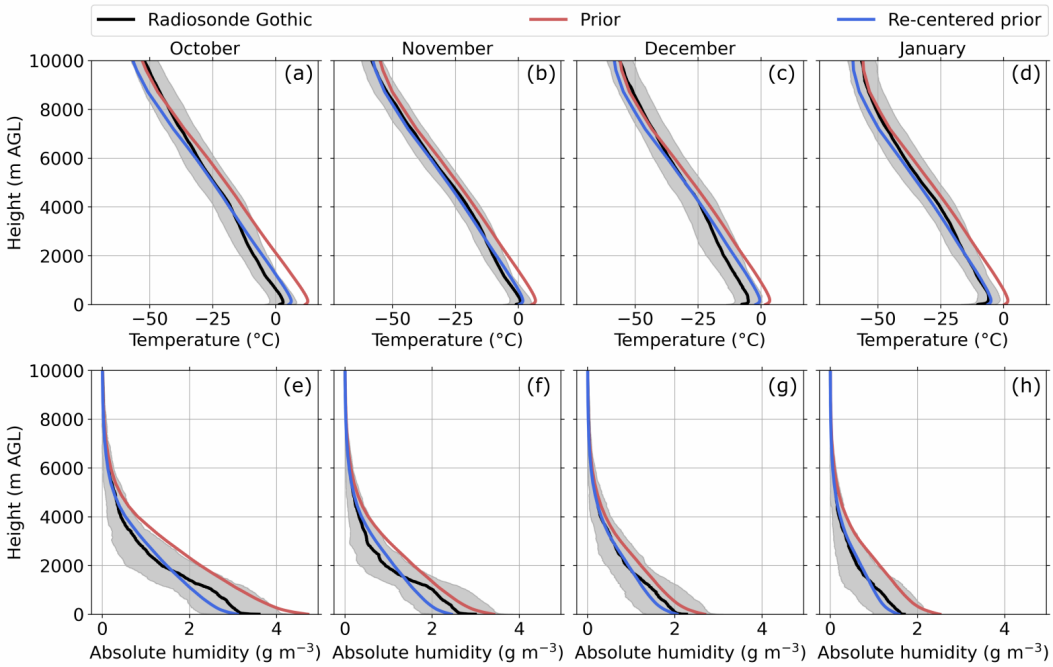

Figure A1. Monthly profiles of (a-d) temperature and (e-h) absolute humidity. The twice daily radiosonde launches at Gothic are averaged for each month with the shading showing the standard deviation. The red line shows the climatological prior computed from radiosonde launches at Denver and the green line shows the profiles after the prior was re-centered using the monthly mean IWV values from the radio soundings at Gothic.

and the ceilometer (NOAA Global Monitoring Laboratory, 2021a) and radiation (NOAA Global Monitoring Laboratory, 2021d) measurements at Brush Creek. NOAA Air Resources Laboratory provided sensible heat flux measurements at Brush Creek. NOAA Physical Science Laboratory conducted the Atmospheric Surface Flux Stations (ASFS) measurements at Avery Picnic and Kettle Ponds (NOAA Physical Science Laboratory, 2021a), and surface meteorology (NOAA Physical Science Laboratory, 2021c), ASSIST (Adler, Bianco, Djalalova, Myers, & Wilczak, 2022), and ceilometer (Adler, Bianco, Djalalova, Myers, Pezoa, et al., 2022) measurements at Roaring Judy. The AERI data at Brush Creek (NOAA National Severe Storms Laboratory, 2021) were collected as part of the Collaborative Lower Atmospheric Profiling System (CLAMPS) by NOAA National Severe Storms Laboratory.

Appendix A Re-centering of the prior

Although radiosondes are launched twice daily at the AMF2 at Gothic, the number of these soundings is not enough to compute the level-to-level covariance for the 110-element state vector of the prior needed for the TROPoe retrievals. Instead, we computed monthly priors using the operational radio soundings launched at Denver, CO, just east of the Rocky Mountains. Although the horizontal distance between the East River Valley and the launch site at Denver is only around 220 km, the elevation difference is 1300 m and the atmospheric conditions can be quite different between the central Rocky Mountains and Denver. To account for differences in the integrated water vapor (IWV) in the atmospheric column due to the elevation difference and to avoid systematic offsets in the prior, we re-centered the mean prior profiles while preserving the relative humidity pro-

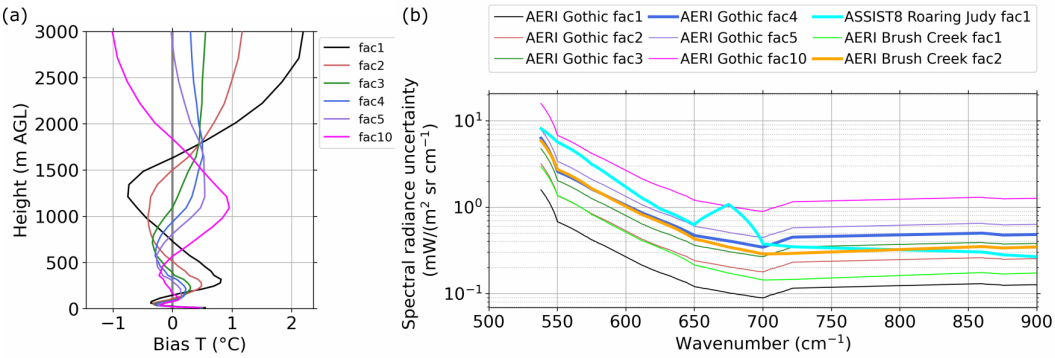

Figure B1. (a) Mean bias between the temperature profiles retrieved with TROPoe for the AERI at Gothic and colocated radio soundings (retrieved profile - radiosonde profile). (b) Mean spectral radiance uncertainty for the AERIs at Gothic and Brush Creek and the ASSIST at Roaring Judy. fac1 indicates that the original uncertainty radiance was used, fac2, fac3, fac4, fac5, and fac10 indicates that the uncertainty radiance was multiplied with a factor of 2, 3, 4, 5, and 10, respectively.

files. We borrowed the concept of recentering from the data assimilation community (e.g. Wang et al., 2013), as TROPoe essentially is a 1-dimensional data assimilation framework. We computed the ratio of the monthly mean IWV from radio soundings at Gothic and the mean IWV of the prior and multiplied the prior mixing ratio profile by this factor. We then adjusted the temperature profile to preserve the relative humidity from the original prior. The re-centered monthly mean prior profiles agreed very well with monthly mean radiosonde profiles at Gothic (Fig. A1).

Appendix B AERI noise modification for TROPoe

The radiance uncertainty of the ARM AERI at Gothic and the CLAMPS AERI at Brush Creek was not large enough to compensate for the missing uncertainty of the forward model in TROPoe which led to unrealistic profiles at Brush Creek and Gothic (temperature inversion always between about 1500 and 2000 m AGL), which indicated an overfitting of the temperature profiles. Figure B1b indicates that the noise of the AERI at Gothic is about a factor of 4 smaller and the noise of the AERI at Brush Creek is about a factor of 2 smaller than the noise of the ASSIST at Roaring Judy. We ran the retrieval for the AERI at Gothic at the time of the radiosonde launches, i.e. at 0 and 12 UTC, for the whole investigation period (92 profiles) and computed the mean differences between the temperature profiles (black line in Fig. B1a). Large differences are visible with a warm bias below around 750 m AGL, a cold bias between 750 m and 1600 m AGL, and a strong warm bias above 1600 m AGL, which is consistent with the unrealistic temperature inversion in the retrieved temperature profiles.

We then systematically increased the noise of the AERI at Gothic by multiplying the spectral radiance uncertainties by the factors 2, 3, 4, 5, and 10 and ran TROPoe with each increased noise level. The spectral radiance uncertainties for the different configurations are shown in Fig. B1b and the resulting temperature bias profiles are shown in Fig. B1a. We decided to use a factor 4 for the AERI at Gothic because (i) the radiance uncertainty was then the same order of magnitude as the ASSIST and (ii) the warm bias above around 1600 m AGL and the cold bias below were much reduced. Even though no radiosonde profiles were available to compare to the retrieved profiles at Brush Creek,

we decided to increase the radiance uncertainty for the AERI there by a factor of 2 to have similar uncertainty radiance values for all three infrared radiometers.

Acknowledgments

We thank all of the individuals, in particular Rocky Mountain Biological Laboratory (RMBL), for help with the SPLASH site selection, leases, instrument deployment and maintenance, data collection, and data quality control. Funding for this work was provided by the NOAA Physical Sciences Laboratory, the U.S. Department of Energy (DOE) Office of Energy Efficiency and Renewable Energy, Wind Energy Technologies Office, and by the NOAA Atmospheric Science for Renewable Energy program. This work was supported by NOAA cooperative agreements NA17OAR4320101 and NA22OAR4320151.

References

Adler, B., Bianco, L., Djalalova, I., Myers, T., Pezoa, S., Bariteau, L., & Wilczak, J. (2022). *NOAA PSL CL31 Ceilometer Backscatter and Cloud Base Height Data for SPLASH* [dataset]. Zenodo. doi: 10.5281/zenodo.7438524

Adler, B., Bianco, L., Djalalova, I., Myers, T., & Wilczak, J. (2022). *NOAA PSL thermodynamic profiles retrieved from ASSIST infrared radiances with the optimal estimation physical retrieval TROPoe during SPLASH* [dataset]. Zenodo. doi: 10.5281/zenodo.7435060

Adler, B., Gohm, A., Kalthoff, N., Babić, N., Corsmeier, U., Lehner, M., ... Georgoussis, G. (2021). CROSSINN: a field experiment to study the three-dimensional flow structure in the Inn Valley, Austria. *Bull. Amer. Meteor. Soc.*, *102*(1), E38–E60. doi: 10.1175/BAMS-D-19-0283.1

Adler, B., & Kalthoff, N. (2014). Multi-scale transport processes observed in the boundary layer over a mountainous island. *Boundary-Layer Meteorol.*, *153*, 515–537. doi: 10.1007/s10546-014-9957-8

Adler, B., Wilczak, J. M., Bianco, L., Djalalova, I., Duncan Jr, J. B., & Turner, D. D. (2021). Observational case study of a persistent cold pool and gap flow in the Columbia River Basin. *J. Appl. Meteor. Climatol.*, *60*(8), 1071–1090. doi: 10.1175/JAMC-D-21-0013.1

Adler, B., Wilczak, J. M., Kenyon, J., Bianco, L., Djalalova, I. V., Olson, J. B., & Turner, D. D. (2022). Evaluation of a cloudy cold-air pool in the Columbia River Basin in different versions of the HRRR model. *EGUsphere*, *2022*, 1–32. doi: 10.5194/egusphere-2022-355

Benjamin, S. G., Smirnova, T. G., James, E. P., Lin, L.-F., Hu, M., Turner, D. D., & He, S. (2022). Land–snow data assimilation including a moderately coupled initialization method applied to NWP. *J. Hydrometeor.*, *23*(6), 825–845. doi: 10.1175/JHM-D-21-0198.1

Benjamin, S. G., Weygandt, S. S., Brown, J. M., Hu, M., Alexander, C. R., Smirnova, T. G., ... others (2016). A North American hourly assimilation and model forecast cycle: The Rapid Refresh. *Mon. Wea. Rev.*, *144*(4), 1669–1694. doi: 10.1175/MWR-D-15-0242.1

Burk, K. (2021). *Balloon-Borne Sounding System (SONDEWNPN).* doi: 10.5439/1595321

Butterworth, B. J., Desai, A. R., Townsend, P. A., Petty, G. W., Andresen, C. G., Bertram, T. H., ... others (2021). Connecting land–atmosphere interactions to surface heterogeneity in CHEESEHEAD19. *Bull. Amer. Meteor. Soc.*, *102*(2), E421–E445. doi: 10.1175/BAMS-D-19-0346.1

Chemel, C., Arduini, G., Staquet, C., Largeron, Y., Legain, D., Tzanos, D., & Paci, A. (2016). Valley heat deficit as a bulk measure of wintertime particulate air pollution in the Arve River Valley. *Atmos. Env.*, *128*, 208–215. doi: 10.1016/j.atmosenv.2015.12.058

Clough, S. A., & Iacono, M. J. (1995). Line-by-line calculation of atmospheric fluxes and cooling rates: 2. application to carbon dioxide, ozone, methane, nitrous oxide and the halocarbons. *J. Geophys. Res.: Atmos.*, *100*(D8), 16519–16535. doi: 10.1029/95JD01386

Clough, S. A., Shephard, M. W., Mlawer, E. J., Delamere, J. S., Iacono, M. J., Cady-Pereira, K., ... Brown, P. D. (2005, March). Atmospheric radiative transfer modeling: a summary of the AER codes. *J. Quant. Spectrosc. Radiat. Transf.*, *91*(2), 233–244. doi: 10.1016/j.jqsrt.2004.05.058

Cox, C. J., Gallagher, M., Shupe, M., Persson, P., Solomon, A., Ayers, T., ... Uttal, T. (2023). Continuous observations of the surface energy budget and meteorology over arctic sea ice during mosaic. *Nature Scientific Data*, *to be submitted*.

Cromwell, E., & Bartholomew, M. (2021). *Weighing Bucket Precipitation Gauge (WBPLUVIO2).* doi: 10.5439/1338194

Cullen, N. J., & Conway, J. P. (2015). A 22 month record of surface meteorology and energy balance from the ablation zone of Brewster Glacier, New Zealand. *J. Glaciol.*, *61*(229), 931–946. doi: 10.3189/2015JoG15J004

Djalalova, I. V., Turner, D. D., Bianco, L., Wilczak, J. M., Duncan, J., Adler, B., & Gottas, D. (2022, January). Improving thermodynamic profile retrievals from microwave radiometers by including radio acoustic sounding system (RASS) observations. *Atmos. Meas. Tech.*, *15*(2), 521–537. doi: 10.5194/amt-15-521-2022

Dowell, D. C., Alexander, C. R., James, E. P., Weygandt, S. S., Benjamin, S. G., Manikin, G. S., ... Alcott, T. I. (2022). The High-Resolution Rapid Refresh (HRRR): An hourly updating convection-allowing forecast model. part i: Motivation and system description. *Wea. Forecasting*, *37*(8), 1371 - 1395. doi: 10.1175/WAF-D-21-0151.1

Duncan Jr., J. B., Bianco, L., Adler, B., Bell, T., Djalalova, I. V., Riihimaki, L., ... Wilczak, J. M. (2022). Evaluating convective planetary boundary layer height estimations resolved by both active and passive remote sensing instruments during the CHEESEHEAD19 field campaign. *Atmos. Meas. Tech.*, *15*(8), 2479–2502. doi: 10.5194/amt-15-2479-2022

Feldman, D., Aiken, A., Boos, W., Carroll, R., Chandrasekar, V., Collins, W., ... Williams, K. (2021). *Surface atmosphere integrated field laboratory (sail) science plan* (Tech. Rep. No. DOE/SC-ARM-21-004). ARM user facility.

Gero, J., Garcia, R., Hackel, D., Ermold, B., & Gaustad, K. (2021). *Atmospheric Emitted Radiance Interferometer (AERICH1).* (Date accessed: 2022-08-21) doi: 10.5439/1025143

Giovannini, L., Laiti, L., Serafin, S., & Zardi, D. (2017). The thermally driven diurnal wind system of the Adige Valley in the Italian Alps. *Quart. J. Roy. Meteor. Soc.*, *143*(707), 2389–2402. doi: 10.1002/qj.3092

Hall, D. K., & Riggs, G. A. (2021). *MODIS/Terra Snow Cover Daily L3 Global 500m SIN Grid, Version 61.* NASA National Snow and Ice Data Center Distributed Active Archive Center. Retrieved 2022-08-21, from `https://nsidc.org/data/MOD10A1/versions/61` (Date accessed: 2022-08-21) doi: 10.5067/MODIS/MOD10A1.061

He, S., Smirnova, T. G., & Benjamin, S. G. (2021). Single-Column validation of a snow subgrid parameterization in the Rapid Update Cycle Land-Surface Model (RUC LSM). *Water Resources Res.*, *57*(8). doi: 10.1029/2021WR029955

Herrera-Mejía, L., & Hoyos, C. D. (2019). Characterization of the atmospheric boundary layer in a narrow tropical valley using remote-sensing and radiosonde observations and the WRF model: the Aburrá Valley case-study. *Quart. J. Roy. Meteor. Soc.*, *145*(723), 2641–2665. doi: 10.1002/qj.3583

Keeler, E., Kyrouac, J., & Ermold, B. (2021). *Automatic Weather Station (MAWS).* doi: 10.5439/1182027

Knuteson, R., Revercomb, H., Best, F., Ciganovich, N., Dedecker, R., Dirkx, T., ... others (2004a). Atmospheric emitted radiance interferometer. Part II: Instrument performance. *J. Atmos. Oceanic Technol.*, *21*(12), 1777–1789. doi: 10.1175/JTECH-1663.1

Knuteson, R., Revercomb, H., Best, F., Ciganovich, N., Dedecker, R., Dirkx, T., ... others (2004b). Atmospheric emitted radiance interferometer. Part I: Instrument design. *J. Atmos. Oceanic Technol.*, *21*(12), 1763–1776. doi: 10.1175/JTECH-1662.1

Lareau, N. P., Crosman, E., Whiteman, C. D., Horel, J. D., Hoch, S. W., Brown, W. O., & Horst, T. W. (2013). The persistent cold-air pool study. *Bull. Amer. Meteor. Soc.*, *94*(1), 51–63. doi: 10.1175/BAMS-D-11-00255.1

Largeron, Y., & Staquet, C. (2016a). The atmospheric boundary layer during wintertime persistent inversions in the Grenoble Valleys. *Front. Earth Sci.*, *4*. doi: 10.3389/feart.2016.00070

Largeron, Y., & Staquet, C. (2016b). Persistent inversion dynamics and wintertime PM10 air pollution in Alpine valleys. *Atmos. Env.*, *135*, 92–108. doi: 10.1016/j.atmosenv.2016.03.045

Lehner, M., Rotach, M. W., & Obleitner, F. (2019). A method to identify synoptically undisturbed, clear-sky conditions for valley-wind analysis. *Boundary-Layer Meteorol.*, *173*(3), 435–450. doi: 10.1007/s10546-019-00471-2

McArthur, L. (2005). *World Climate Research Programme - Baseline Surface Radiation Network (BSRN)-Operations Manual Version 2.1.* Experimental Studies Division, Atmospheric Environment Service. Retrieved from `https://library.wmo.int/index.php?lvl=notice_display&id=11762`

Morris, V., Zhang, D., & Ermold, B. (2021). *Ceilometer (ceil).* doi: 10.5439/1181954

Mott, R., Vionnet, V., & Grünewald, T. (2018). The seasonal snow cover dynamics: review on wind-driven coupling processes. *Front. Earth Sci.*, *6*, 197. doi: 10.3389/feart.2018.00197

NOAA Global Monitoring Laboratory. (2021a). *Ceilometer CL51 Brush Creek* [dataset]. Retrieved 2022-11-16, from `https://gml.noaa.gov/aftp/g-rad/surfrad/ceilometer/cl51_cloud_prod_lev0/cbc/`

NOAA Global Monitoring Laboratory. (2021b). *Ceilometer CL51 Kettle Ponds* [dataset]. Retrieved 2022-11-16, from `https://gml.noaa.gov/aftp/g-rad/surfrad/ceilometer/cl51_cloud_prod_lev0/ckp/`

NOAA Global Monitoring Laboratory. (2021c). *Radiation and surface meterological station Brush Creek* [dataset]. Retrieved 2022-11-16, from `https://gml.noaa.gov/aftp/data/radiation/campaigns/Format/ckp/`

NOAA Global Monitoring Laboratory. (2021d). *Radiation and surface meterological station Brush Creek* [dataset]. Retrieved 2022-11-16, from `https://gml.noaa.gov/aftp/data/radiation/campaigns/Format/cbc/`

NOAA National Severe Storms Laboratory. (2021). *Collaborative Lower Atmospheric Profiling System Brush Creek* [dataset]. Retrieved 2022-11-16, from `https://data.nssl.noaa.gov/thredds/catalog/FRDD/CLAMPS/clamps/clamps2/ingested/catalog.html`

NOAA Physical Science Laboratory. (2021a). *Atmospheric Surface Flux Statinos (ASFS)* [dataset]. Retrieved 2022-11-16, from `ftp://ftp1.esrl.noaa.gov/Observations/Campaigns/SPLASH/`

NOAA Physical Science Laboratory. (2021b). *SPLASH - Study of Precipitation, the Lower Atmosphere, and Surface for Hydrometeorology* [website]. Retrieved 2022-08-04, from `https://psl.noaa.gov/splash/`

NOAA Physical Science Laboratory. (2021c). *Surface meterological station Roaring Judy* [dataset]. Retrieved 2022-11-16, from `https://psl.noaa.gov/data/obs/sites/view_site_details.php?siteID=rjy`

Obleitner, F. (1994). Climatological features of glacier and valley winds at the

Hintereisferner (Ötztal Alps, Austria). *Theor. Appl. Climatol.*, *49*(4), 225–239. Retrieved 2022-09-09, from http://link.springer.com/10.1007/BF00867462 doi: 10.1007/BF00867462

Rochette, L., Smith, W. L., Howard, M., & Bratcher, T. (2009). ASSIST, Atmospheric Sounder Spectrometer for Infrared Spectral Technology: latest development and improvement in the atmospheric sounding technology. In *Imaging spectrometry xiv* (Vol. 7457, pp. 9–17). doi: 10.1117/12.829344

Sedlar, J., Meyers, T., Adler, B., & Cox, C. (n.d.). Low-level liquid-bearing clouds drive lower atmosphere stability and surface energy forcing over a seasonally snow-covered high-mountain watershed environment.

Sedlar, J., Riihimaki, L., Turner, D., Duncan, J., Adler, B., Bianco, L., ... others (2022). Investigating the impacts of daytime boundary layer clouds on surface energy fluxes and boundary layer structure during CHEESEHEAD19. *J. Geophys. Res.*, *127*(5), e2021JD036060. doi: 10.1029/2021JD036060

Seibert, P., Beyrich, F., Gryning, S.-E., Joffre, S., Rasmussen, A., & Tercier, P. (2000). Review and intercomparison of operational methods for the determination of the mixing height. *Atmos. Env.*, *34*(7), 1001–1027. doi: 10.1016/S1352-2310(99)00349-0

Serafin, S., Adler, B., Cuxart, J., De Wekker, S., Gohm, A., Grisogono, B., ... others (2018). Exchange processes in the atmospheric boundary layer over mountainous terrain. *Atmosphere*, *9*(3), 102. doi: 10.3390/atmos9030102

Shi, Y. (2021a). *Ground Radiometers on Stand for Upwelling Radiation (GNDRAD60S).* (Date accessed: 2022-08-21) doi: 10.5439/1377837

Shi, Y. (2021b). *Sky Radiometers on Stand for Downwelling Radiation (SKYRAD60S).* (Date accessed: 2022-08-21) doi: 10.5439/1377836

Skamarock, W. C. (2004, December). Evaluating mesoscale NWP models using kinetic energy spectra. *Mon. Wea. Rev.*, *132*(12), 3019–3032. Retrieved 2022-09-11, from http://journals.ametsoc.org/doi/10.1175/MWR2830.1 doi: 10.1175/MWR2830.1

Skamarock, W. C., & Klemp, J. B. (2008, March). A time-split nonhydrostatic atmospheric model for weather research and forecasting applications. *J. Comput. Phys.*, *227*(7), 3465–3485. Retrieved 2022-09-11, from https://linkinghub.elsevier.com/retrieve/pii/S0021999107000459 doi: 10.1016/j.jcp.2007.01.037

Smirnova, T. G., Brown, J. M., Benjamin, S. G., & Kenyon, J. S. (2016). Modifications to the Rapid Update Cycle Land Surface Model (RUC LSM) available in the Weather Research and Forecasting (WRF) Model. *Mon. Wea. Rev.*, *144*(5), 1851–1865. doi: 10.1175/MWR-D-15-0198.1

Song, Y., Zhu, T., Cai, X., Lin, W., & Kang, L. (2007). Glacier winds in the Rongbuk Valley, north of Mount Everest: 1. Meteorological modeling with remote sensing data. *J. Geophys. Res.*, *112*(D11), D11101. doi: 10.1029/2006JD007867

Stigter, E. E., Steiner, J. F., Koch, I., Saloranta, T. M., Kirkham, J. D., & Immerzeel, W. W. (2021). Energy and mass balance dynamics of the seasonal snowpack at two high-altitude sites in the Himalaya. *Cold Regions Science and Technology*, *183*, 103233. doi: 10.1016/j.coldregions.2021.103233

Stull, R. B. (1988). *An introduction to boundary layer meteorology.* Dordrecht, The Netherlands: Kluwer Academic Publishers, 666 pp.

Sullivan, R., Billesbach, D., Keeler, E., & Ermold, B. (2021). *Eddy Correlation Flux Measurement System (30ECOR).* doi: 10.5439/1025039

Turner, D. D., & Blumberg, W. G. (2019). Improvements to the AERIoe thermodynamic profile retrieval algorithm. *IEEE Journal of Selected Topics in Applied Earth Observations and Remote Sensing*, *12*(5), 1339–1354. doi: 10.1109/JSTARS.2018.2874968

Turner, D. D., Knuteson, R. O., Revercomb, H. E., Lo, C., & Dedecker, R. G.

(2006). Noise reduction of Atmospheric Emitted Radiance Interferometer (AERI) observations using principal component analysis. *J. Atmos. Oceanic Technol.*, *23*(9), 1223–1238. doi: 10.1175/JTECH1906.1

Turner, D. D., & Löhnert, U. (2021). Ground-based temperature and humidity profiling: combining active and passive remote sensors. *Atmos. Meas. Tech.*, *14*(4), 3033–3048. doi: 10.5194/amt-14-3033-2021

Turner, D. D., & Löhnert, U. (2014, 03). Information content and uncertainties in thermodynamic profiles and liquid cloud properties retrieved from the ground-based atmospheric emitted radiance interferometer (AERI). *J. Appl. Meteor. Climatol.*, *53*(3), 752-771. doi: 10.1175/JAMC-D-13-0126.1

Wagner, T. J., Klein, P. M., & Turner, D. D. (2019). A new generation of ground-based mobile platforms for active and passive profiling of the boundary layer. *Bull. Amer. Meteor. Soc.*, *100*(1), 137–153. doi: 10.1175/BAMS-D-17-0165.1

Wang, X., Parrish, D., Kleist, D., & Whitaker, J. (2013). GSI 3DVar-based ensemble–variational hybrid data assimilation for NCEP Global Forecast System: Single-resolution experiments. *Mon. Wea. Rev.*, *141*(11), 4098–4117. doi: 10.1175/MWR-D-12-00141.1

Whiteman, C. D. (1982). Breakup of temperature inversions in deep mountain valleys. *J. Appl. Meteor.*, *21*, 270–289. doi: 10.1175/1520-0450(1982)021⟨0270:BOTIID⟩2.0.CO;2

Whiteman, C. D. (2000). *Mountain meteorology fundamentals and applications*. New York: Oxford University Press, 355 pp.

Whiteman, C. D., Bian, X., & Zhong, S. (1999). Wintertime evolution of the temperature inversion in the Colorado Plateau Basin. *J. Appl. Meteor.*, *38*(8), 1103–1117. doi: 10.1175/1520-0450(1999)038⟨1103:WEOTTI⟩2.0.CO;2

Xu, Z., Siirila-Woodburn, E. R., Rhoades, A. M., & Feldman, D. (2022). Sensitivities of subgrid-scale physics schemes, meteorological forcing, and topographic radiation in atmosphere-through-bedrock integrated process models: A case study in the Upper Colorado River Basin. *EGUsphere*, *2022*, 1–29. doi: 10.5194/egusphere-2022-437

Zardi, D., & Whiteman, C. D. (2013). Diurnal mountain wind systems. In F. K. Chow, S. F. J. De Wekker, & B. J. Snyder (Eds.), *Mountain weather research and forecasting* (pp. 35–119). Dordrecht: Springer.

Zhong, S., & Chow, F. K. (2013). Meso- and fine-scale modeling over complex terrain: Parameterizations and applications. In F. K. Chow, S. F. De Wekker, & B. J. Snyder (Eds.), *Mountain weather research and forecasting: Recent progress and current challenges* (pp. 591–653). Dordrecht: Springer Netherlands. doi: 10.1007/978-94-007-4098-3_10